ACS OMEGA

http://pubs.acs.org/journal/acsodf

Article

Theoretical and Experimental Study of CaMgSi Thermoelectric Properties

Jesus L. A. Ponce-Ruiz,* Seiya Ishizuka, Yoshikazu Todaka, Yuki Yamada, Armando Reyes Serrato, and J. M. Herrera-Ramirez*

Cite This: *ACS Omega* 2022, 7, 15451−15458

Read Online

ACCESS | Metrics & More | Article Recommendations

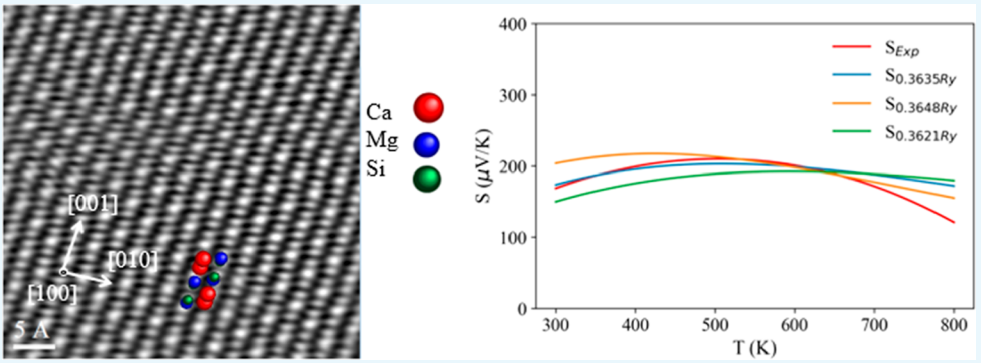

ABSTRACT: Pure CaMgSi was successfully synthesized by mechanical milling, followed by spark plasma sintering. Rietveld refinement was used to calculate the structural parameters, where a crystallite size (D_{XRD}) of 79 nm was estimated. This value was confirmed by the Williamson−Hall analysis. Transmission electron microscopy was used to analyze the microstructure, revealing the presence of extensive interfaces, nanoparticles, and a high crystallinity. First-principles calculations were performed with the WIEN2k package, finding a band gap of 0.27 eV. The thermoelectric properties were determined combining experimental measurements and theoretical results from the BoltzTraP code. The highest value of the electronic figure of merit (ZT_e) was 1.67 at 415 K. However, when the lattice thermal contribution (k_L) is considered, the highest value of the figure of merit (ZT) was 0.144 at 644 K.

1. INTRODUCTION

Thermoelectricity is the phenomenon in which heat is directly converted into electrical energy making use of the Seebeck effect. This makes it possible to utilize the wasted heat from industrial processes or transport. Thermoelectric materials can be used to form thermoelectric generators stacking p−n semiconductors without the need of moving parts and low maintenance is required. However, despite their benefits, the mass application of these devices has been limited by their low efficiency, the cost of the materials, and the toxicity of some of their constituent elements. The conversion efficiency of thermoelectric (TE) materials is related to a quantity called figure of merit (ZT), which is defined in eq 1.

$$ZT = \frac{S^2\sigma T}{k} = \frac{\mathrm{PFT}}{k} = \frac{S^2 T}{k\rho} = \frac{S^2 T}{(k_e + k_L)\rho} \quad (1)$$

where S is the Seebeck coefficient, σ is the electrical conductivity, T is the absolute temperature, PF is the power factor equivalent to $S^2\sigma$, ρ is the electrical resistivity, and k is the thermal conductivity, which have contributions from electrons (k_e) and the crystal lattice (k_L). On the other hand, eq 2 defines the electronic TE figure of merit (ZT_e). Note that ZT_e is always greater than ZT because k_L is not considered. ZT_e can be used to estimate how good a promising candidate is for TE applications.[1] In semiconductors, the main source of thermal conductivity is the phonon contribution of k_L, so it must be considered.

$$ZT_e = \frac{S^2 T}{k_e \rho} \quad (2)$$

In order to find new TE materials, two approaches have been used: first, to explore materials with an intrinsic high ZT and second, to optimize TE properties of a known material by a physical modification.[2,3] Kagdada et al. used the first

Received: December 27, 2021
Accepted: April 19, 2022
Published: April 28, 2022

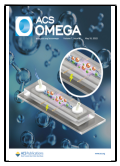

approach and calculated the TE properties of GeTe with the first-principles calculation plus the BoltzTraP code, obtaining ZT = 0.7 at 1300 K, while Reyes et al. obtained ZT = 0.8 for ReCN at 1200 K.[4,5] On the other hand, using the second approach, Haque and Rahaman explored the TE behavior of BaGaSnH, replacing Ba by Sr using first-principles calculations and the BoltzTraP code, predicting a $ZT \sim 1.0$.[6] Hong et al. were able to maximize the ZT value of GeTe by doping with Sb and Se, reaching a value of ZT = 2.20 at 780 K.[7] Hicks and Dresselhaus proposed increasing the ZT by preparing multilayered superlattice materials.[8] For the case of SiGe compounds, p-type and n-type and the influence of nanostructuring over the TE properties have been reported.[9−11] Thin films made of $AgPb_{18}SbTe_{20}$ were synthesized by molecular beam epitaxy, obtaining ZT = 2.1 at 800 K; however, this synthesis process is slow and expensive, making it difficult to manufacture on a large scale.[12] Bi_2Te_3-based materials have been the most widely studied for TE applications. Poudel et al. made nanocomposites with the addition of Sb by mechanical milling (MM) and hot pressing (HP), reaching a value of ZT = 1.4 at 373 K, which is a good value for low-temperature applications, but it could still be improved.[13] Consolidating milled powders by the spark plasma sintering (SPS) technique has several advantages over HP since SPS was originally designed to inhibit the grain size and provide a better densification.[14] The phase diagram of Ca−Mg−Si was calculated by Gröbner et al. using the Calphad method.[15] The potential applications of CaMgSi have motivated studies in the field of hydrogen storage and biodegradable implants.[16−18] Besides, the electronic structure information presented by Whalen et al. suggests the CaMgSi compound as a possible candidate for TE applications.[16] However, obtaining a pure phase is a difficult task by conventional synthesis methods. TE properties of Ca−Mg−Si alloys were presented by Niwa et al., obtaining a maximum of 37% CaMgSi, 53% Mg_2Si, and 10% $Ca_7Mg_{7.25}Si_{14}$.[19] CaMgSi, synthesized by MM and SPS, is a promising candidate for TE applications, and even with several secondary phases, it obtained a value of PF = 0.42 mW m^{-1} K^{-2} at 433 K; however, thermal conductivity and ZT were not determined.[20] Theoretical simulation using first-principles and Boltzmann transport theory have been used to predict the ZT of CaMgSi by tuning the carrier concentration, reaching a value of ZT = 1.75 at 800 K.[21] The present work aims to determine the structure, microstructure, and TE properties of an experimental sample of CaMgSi compound by combining theoretical simulation and experimental measurements.

2. RESULTS AND DISCUSSION

2.1. X-ray Diffraction. Figure 1 shows the refined X-ray diffraction (XRD) pattern of CaMgSi synthesized by MM and SPS, where the signals of pure CaMgSi with the space group *Pnma* (PDF #43-1399) were observed. It is worth mentioning that pure CaMgSi has not been reported previously. In this case, this finding can be attributed to the rotational speed of 180 rpm under the MM conditions, which guaranteed a better homogeneity than that obtained by Miyazaki et al., who used 125 rpm and obtained six secondary phases.[22] Obtaining pure phases makes it possible to compare the experimental measurements with the simulation. Rietveld refinement was performed to determine the lattice parameters (a, b, c, α, β, γ), the crystallite size (D_{XRD}), atomic positions (x, y, z),

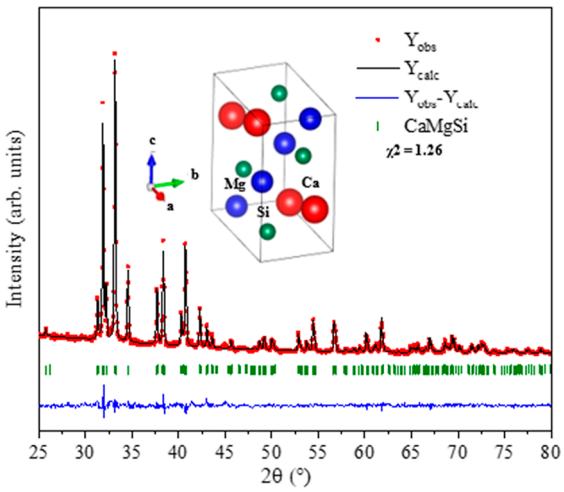

Figure 1. XRD pattern of CaMgSi synthesized by MM and SPS.

occupation factor (g), volume cell (V), and density (ρ). Table 1 summarizes the values calculated.

Figure 2 shows the Williamson−Hall analysis, with which microstrains (ε) and crystallite size were calculated.[23] A crystallite size of 79 nm was determined, which is practically the same as the one found by the Rietveld refinement. The crystallite size is small enough to contribute to the reduction of the lattice thermal conductivity (k_L) by increasing phonon scattering and acting as a nanostructured bulk material.[13] The density of dislocations (δ) was determined by the Williamson−Smallman relation $\delta = 1/D^2$.[24] Table 1 presents these values.

2.2. Transmission Electron Microscopy. Figure 3a shows a transmission electron microscopy (TEM) micrograph, where several grain boundaries are observed. Figure 3b shows a high-resolution TEM image in which the presence of a spherical nanoparticle is identified. A similar morphology was reported by Minnich et al. for nanostructured TE materials.[9] The high density of interfaces and the presence of nanoparticles reduces the thermal conductivity and increases the ZT according to eq 1.[12,13] Figure 3c shows a region with high crystallinity, where CaMgSi exhibits an orthorhombic arrangement, which is consistent with the *Pnma* structure oriented in the [100] direction. Figure 3d presents a selected area electron diffraction (SAED) pattern showing sharp and bright diffraction spots, which were assigned to the well-crystallized orthorhombic phase of CaMgSi, and a [100] zone axis was confirmed.

2.3. First-Principles Calculation. The structural parameters reported in Table 1 were used to calculate the optimization of CaMgSi; a = 7.4460 Å, b = 4.4224 Å, c = 8.2950 Å, and a volumetric reduction of 0.29% were obtained. Figure 4a shows the calculated density of states (DOS) determined by the WIEN2k package using the Tran−Blaha modified Becke Johnson (TB-mBJ) potential for the exchange−correlation, obtaining a band gap value of 0.27 eV. It is well documented that using the TB-mBJ improves the band gap calculation of different semiconductors compared to other approximations such as local density approximation and general gradient approximation (GGA) that usually underestimate the band gap.[25] Figure 4b shows a strong hybridization between Ca d−Si p and Mg p−Si d, which is consistent with results previously reported using different potentials.[20,21] Figure 5 shows the calculated band structure with TB-mBJ that confirms a direct band gap in the gamma direction. Miyasaki et

https://doi.org/10.1021/acsomega.1c07307
ACS Omega 2022, 7, 15451−15458

Table 1. Parameters Calculated by Rietveld, Williamson–Hall, and TEM Analysis

a (Å)	b (Å)	c (Å)	$\alpha = \beta = \gamma$ (deg)	D_{XRD} (nm)	D_{TEM} (nm)	ε	δ (cm^{-2})
7.4764(18)	4.4264(12)	8.3014(2)	90.0	79.02	110	1.21×10^{-3}	1.601×10^{10}
atom	site	x	y	z		g	B
Ca	4c	0.0189(5)	0.2500	0.6809(4)		1.00219	1.0573
Mg	4c	0.1432(7)	0.2500	0.0656(7)		0.96110	0.5407
Si	4c	0.2690(6)	0.2500	0.3842(5)		0.99767	0.8511

V = 274.730(12) Å^3, ρ = 2.209 g/cm^3

reliability factors: R_p = 5.78%, R_{wp} = 7.62%, R_e = 6.79%, R_B = 5.79%, R_F = 7.69%

goodness-of-fit indicator: $S = R_{wp}/R_e$ = 1.122

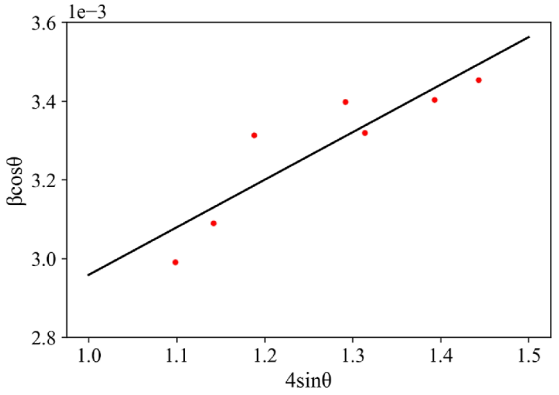

Figure 2. Williamson–Hall plot analysis for the CaMgSi lattice.

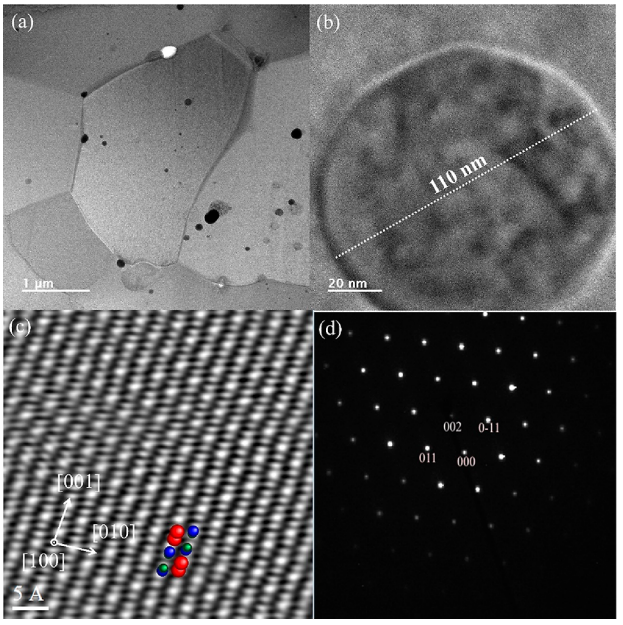

Figure 3. TEM images showing the microstructure of CaMgSi: (a) micrometric grains with clear grain boundaries, (b) high-resolution image showing a nanoparticle, (c) high-crystallinity zone, and (d) indexed SAED pattern with the [100] zone axis.

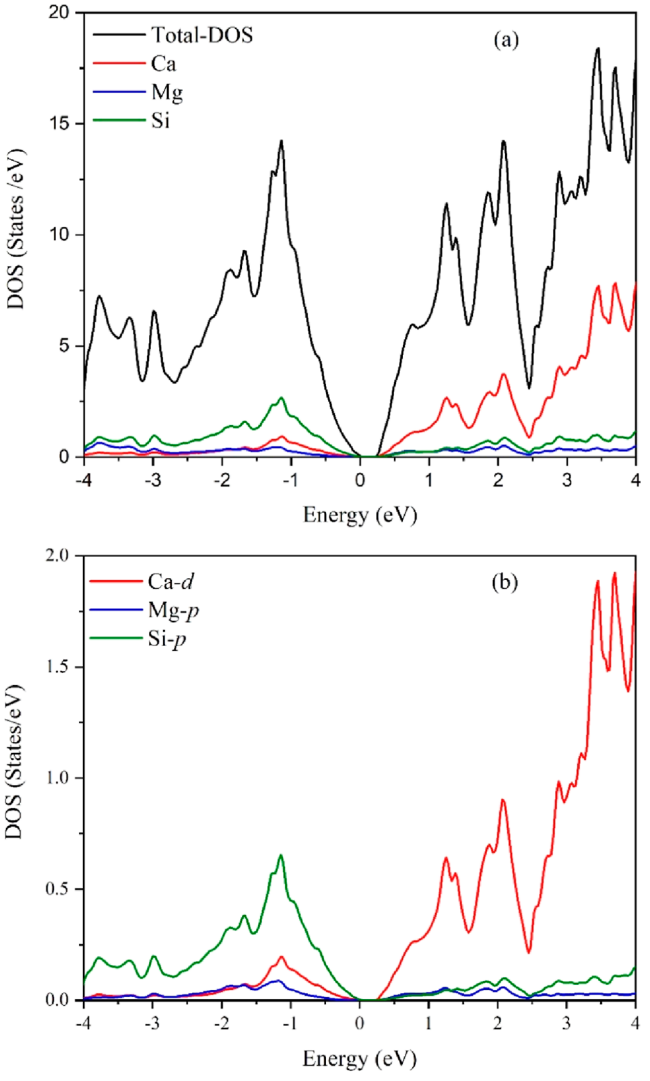

Figure 4. DOS of CaMgSi calculated using WIEN2k with TB-mBJ (a) total and (b) partial.

al. used the WIEN2k package and a GGA, reporting a band gap of 0 eV. Besides, they determined a narrow band gap of 0.26 eV by photoemission spectrum, which showed a clear inconsistency between the first-principles calculations and the experimental results.[22] Yang et al. calculated the electronic properties using the Vienna ab initio simulation package (VASP) applying the hybrid functional Heyd–Scuseria–Ernzerhof (HSE06), obtaining a direct band gap of 0.29 eV.[21]

2.4. TE Properties. TE properties were calculated by BoltzTraP once the theoretical band gap matched with the experimental values.[26] Figure 6 shows the simulated value of S as a function of μ at different temperatures (300–800 K) for the CaMgSi compound. In the case of the p-type doping, the maximum S value was 286 μV at 0.3691 Ry, while in n-type doping, it was −372 μV at 0.3759 Ry for a fixed temperature of 300 K. Besides, the transition from p-type to n-type was observed at a μ of 0.3724 Ry. Most of the theoretical reports of TE materials such as PbSe, SnSe, GeSe, and hybrid perovskites

https://doi.org/10.1021/acsomega.1c07307
ACS Omega 2022, 7, 15451−15458

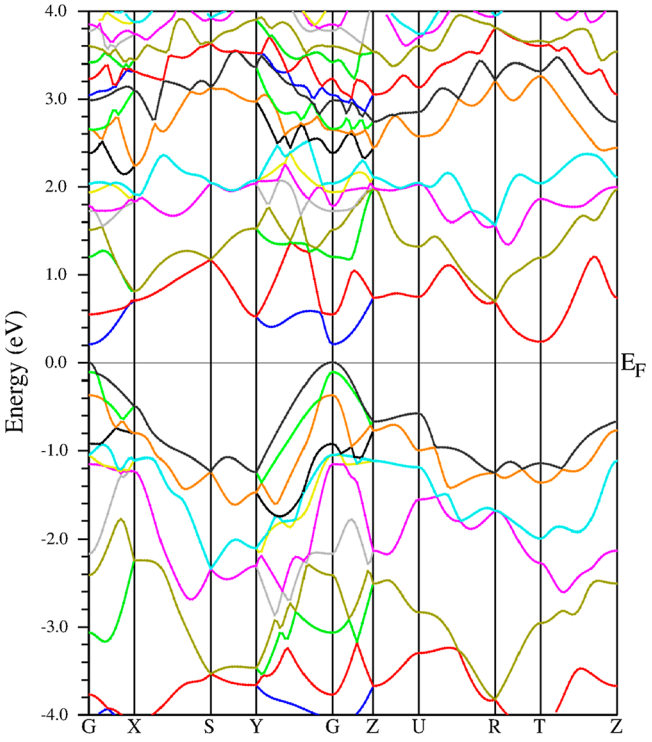

Figure 5. Calculated band structure of CaMgSi using WIEN2k with the TB-mBJ potential.

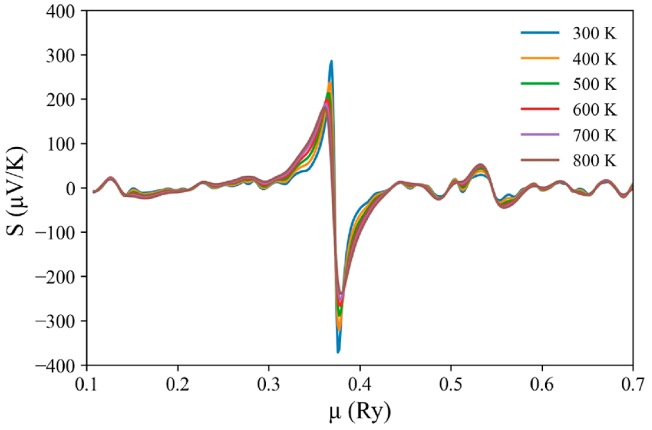

Figure 6. Seebeck coefficient (S) of CaMgSi as a function of the chemical potential (μ) at different temperatures.

$CH_3CH_2NH_3GeI_3$ use the μ that describes the best properties.[27,28]

In our case, the μ determined is the one that best describes the S experimental value (S_{Exp}) since it will represent the TE properties on the synthesized CaMgSi. Figure 7 shows the Seebeck values as a function of the temperature. The red line represents the S_{Exp} obtained from ZEM-1, while the other lines represent the three closest theoretical Seebeck (S_T) values obtained at a fixed μ. A python code was developed to make a semiempirical adjustment by the least squares method, in which the S_T, S_{Exp}, theoretical slope, and experimental slope at fixed μ were considered. The S_T value at a μ of 0.3635 Ry is the one that best describes the S_{Exp} (blue line). This fitting method to find a μ that describes the experimental values has been used by Hayashi et al. for single-wall carbon nanotubes.[29] This semi-

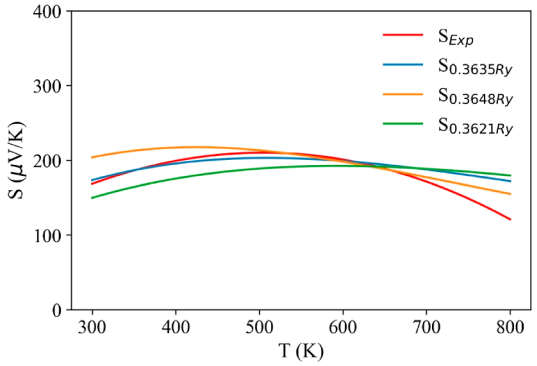

Figure 7. Semi-empirical adjustment from the Seebeck coefficient of CaMgSi to determine the chemical potential.

empirical method has been previously described by Prashun et al.[1]

Figure 8a shows the simulated properties σ/τ, and Figure 8b shows k_e/τ as a function of the temperature for the determined

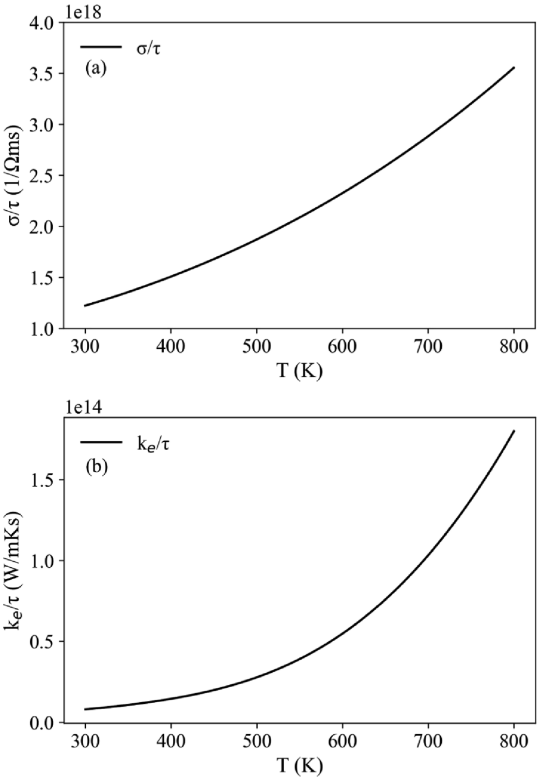

Figure 8. Obtained conductivities of CaMgSi: (a) electrical conductivity σ/τ and (b) thermal conductivity k_e/τ.

μ = 0.3635 Ry. An increase is observed in both properties as the temperature increases.

Figure 9a shows the experimental conductivity (σ_{Exp}), and Figure 9b shows the relaxation time (τ) as a function of the temperature, which were determined by $\tau = \sigma_{Exp}/(\sigma/\tau)$. As can be seen, τ decreases as the temperature increases until stabilizing at a value of 0.44×10^{-14} s. The determination of the relaxation time using this methodology has been reported by Kumar et al.[30]

In order to determine the nature of the lattice thermal conductivity, the phonon band structure and phonon DOS were determined (Figure 10). It can be noted that all bands

https://doi.org/10.1021/acsomega.1c07307
ACS Omega 2022, 7, 15451−15458

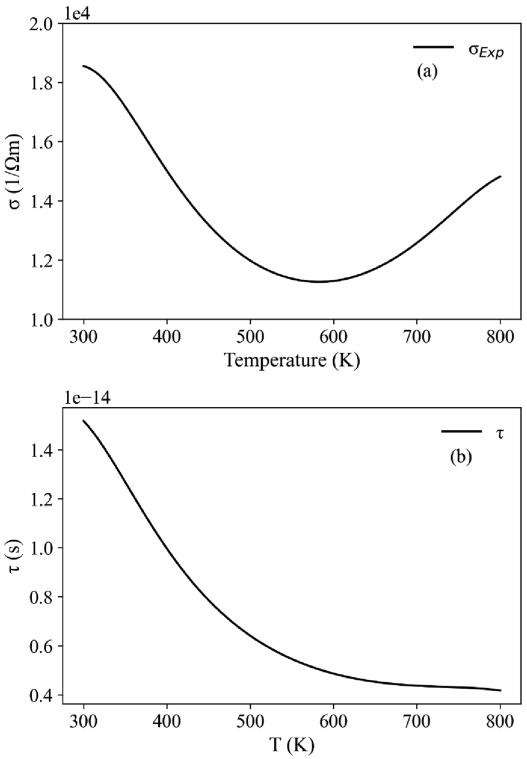

Figure 9. (a) Experimental electrical conductivity σ_{Exp} of CaMgSi and (b) relaxation time τ obtained from the experimental and theoretical electrical conductivities.

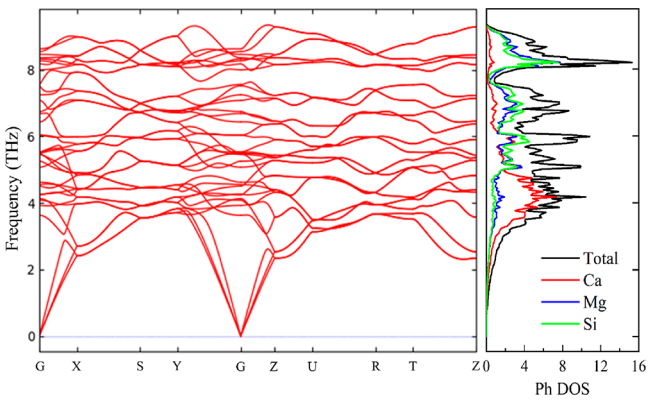

Figure 10. Calculated phonon band structure and phonon DOS of CaMgSi.

start above 0 THz, showing dynamical stability. The CaMgSi unit cell contains 12 atoms, which generate 3 acoustic branches (TA1, TA2, and LA) and 33 optical branches in the first Brillouin zone. The low values of the acoustic branches (0−2.5 THz) suggest a low k_L. The Ph DOS shows that the vibration modes of Mg and Si are strongly coupled due to their similar mass. The high optical frequency modes are precented above 8 THz produced mainly by Mg and Si. The phonon properties of CaMgSi synthesized in this work are consistent with those reported by Yang et al.[21]

Figure 11a shows the Grüneisen parameter (γ) of CaMgSi as a function of the frequency, which represents the degree of anharmonicity.[31] The acoustic phonon modes (0−2.5 THz) provide γ values of −1.2 to 4.2. Figure 11b shows the lifetime of CaMgSi obtaining a value of 16.8 ps at acoustic branches. Li et al. reported similar values of the Grüneisen parameter and lifetime for BaMgSi, $Ba_2Mg_3Si_4$, and $BaMg_2Si_2$, identifying that they can be designed as low-thermal-conductivity materials.[32]

Figure 12a shows the electronic contribution to the thermal conductivity k_e, which was determined with the BoltzTraP package at a chemical potential of μ = 0.3635 Ry and by taking the obtained relaxation time. Figure 12b shows the lattice contribution to the thermal conductivity k_L, which was obtained combining density functional theory (DFT) calculations implemented in the VASP and phono3py.[33−35] Figure 12 proves that k_L is several times bigger than k_e; thus, k_L must be reduced to increase ZT. It is important to consider the influence of the density of dislocations δ in Table 1 because it can reduce k_L reported in Figure 12b through phonon scattering.[36,37]

Figure 13a shows the ZT_e value as a function of the temperature, reaching a maximum value of ZT_e = 1.67 at 415 K. Figure 13b shows the ZT value considering the effect of k_L, for which the values are lower than for ZT_e, but reaching a maximum value of ZT = 0.144 at 644 K. Table 2 shows a summary of the TE properties obtained in this work. The biggest difference between the values presented in Table 2 and those simulated (ZT = 1.78 at 800 K) can be mainly attributed to the fact that the experimental electrical conductivity σ_{Exp} is several times lower than the one predicted by Yang et al.[21] The presented information suggests that increasing σ will lead to bigger ZT values, which can be achieved by doping the CaMgSi compound.

3. CONCLUSIONS

In the presented work, pure CaMgSi was successfully synthesized using MM followed by SPS, obtaining a crystallite size of 79 nm. The morphology reported confirms the formation of a nanostructured bulk material with a high crystallinity. Through first-principles calculations, a band gap of 0.27 eV was obtained, which is very close to the experimental value of 0.26 eV. The thermal conductivity and relaxation time were obtained combining BoltzTraP results with experimental measurements, making it possible to determine the figure of merit, with a maximum value of ZT_e = 1.67 at 415 K. When k_L was included, a maximum value of ZT = 0.144 at 644 K was obtained. However, the experimental electrical conductivity σ_{Exp} obtained is several times lower than the one previously simulated, the increment of σ_{Exp} being the key factor to reach bigger values of ZT.

4. EXPERIMENTAL CONDITIONS AND COMPUTATIONAL METHODS

4.1. Experimental Procedure. CaH_2 (Sigma-Aldrich 99%, <200 μm), Mg (Mitsuwa chemicals 99.9%, <150 μm), and Si (Kojundo Chemicals, 99.9%, <5 μm) were used to synthesize the CaMgSi compound. Initially, 100 g of precursor powders was weighed in a stoichiometric ratio into a glovebox under an Ar atmosphere. Then, the powders were mechanically milled under an Ar atmosphere using a planetary ball mill (Pulverisette 5); a 500 cm^3 bowl (SUS304 stainless steel) and 100 bearing balls (SUJ2 bearing steel, 10 mm) were used. The ball-to-powder weight ratio was 4:1, the rotational speed of the main disk was 180 rpm, and the powders were milled for 20 h to obtain a better homogeneity. The milled powders (5 g) were put into a graphite die with an inner diameter of 25 mm and a thickness of 4 mm. Subsequently, an SPS machine (Dr. Sinter SPS, Sumitomo Coal Mining) was utilized under an Ar

https://doi.org/10.1021/acsomega.1c07307
ACS Omega 2022, 7, 15451−15458

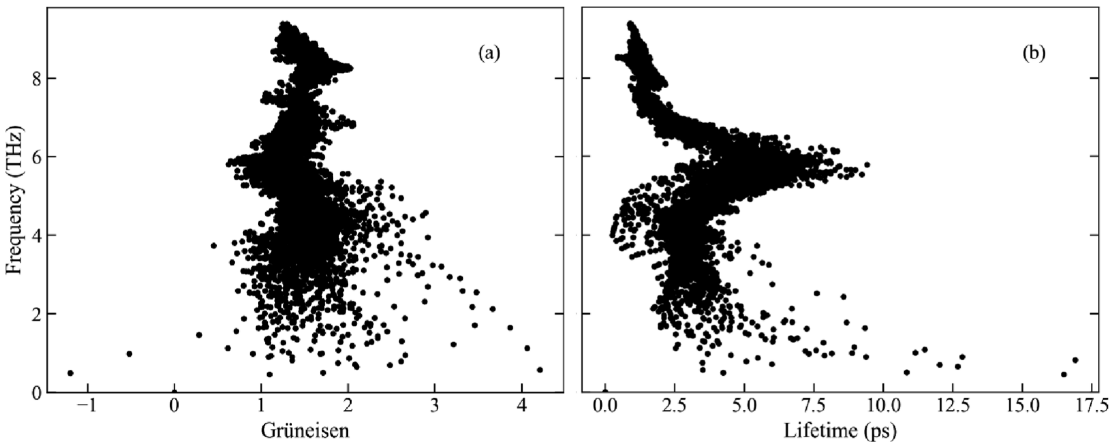

Figure 11. (a) Grüneisen parameter and (b) lifetime of CaMgSi.

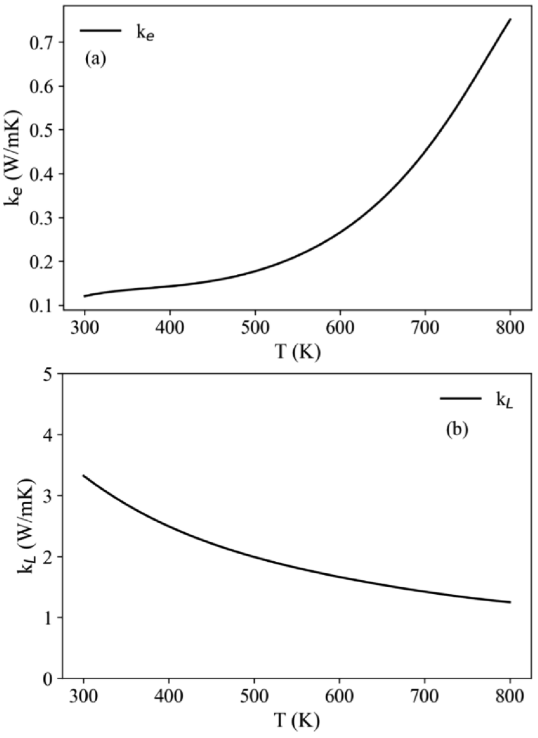

Figure 12. Thermal conductivities of CaMgSi due to (a) electrons obtained from relaxation time and BolzTraP and (b) lattice obtained from phono3py.

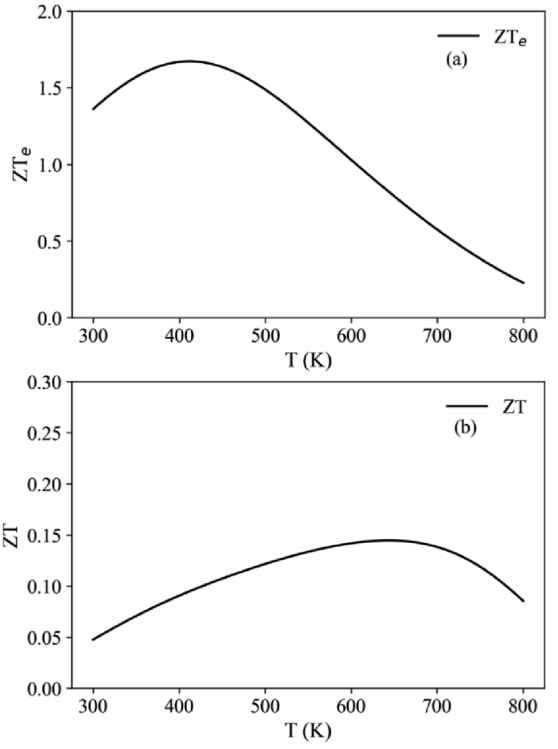

Figure 13. *ZT* of CaMgSi as a function of the temperature: (a) electronic contribution ZT_e and (b) total *ZT*.

atmosphere and a constant pressure of 50 MPa. The SPS conditions used in this case were taken from Miyazaki et al.[20] Thus, the milled powders were sintered at 1273 K for 20 min with a heating ramp of 97.5 K/min (dehydrogenation of CaH_2 and formation of CaMgSi). Then, a controlled cooling was carried out with a ramp of 33.3 K/min up to a temperature of 773 K. Later, a natural cooling up to room temperature was done.

4.2. Characterization. Powder XRD patterns of CaMgSi powders were acquired with a PANalytical X'Pert Pro diffractometer equipped with a monochromator and a radiation source of Cu Kα1 (λ_1 = 1.54056 Å) operating at 40 kV/30 mA. Diffraction patterns were acquired in the 2θ range of 25−80° with a step size of 0.02°. Rietveld refinement was performed using FullProf software, and the crystal structure was generated with the VESTA software.[38−40] TEM micrographs were obtained with a JEOL JEM2200FS +CS microscope at an accelerating voltage of 200 kV. The Miller indices' identification on the SAED patterns was made with the Crystallographic Tool Box (CrysTBox) software using the z.[41] The experimental TE measurements were taken with a ZEM-1 Ulvac Sinku-Riko equipment.

4.3. Computational Details. The first-principles calculations were done with the WIEN2k package, which allows us to perform electronic structure calculations using the DFT. It is based on the full-potential linearized augmented plane wave method for solving Kohn−Sham equations.[42] The exchange−correlation energy was treated with the TB-mBJ potential.[25] The separation energy between the core and the valence state was set to −6.0 Ry. Our calculations were carried out in the Brillouin zone with a 13 × 23 × 12 uniform *k*-point mesh and a convergence criterion of 10^{-4} Ry. The TE properties were

https://doi.org/10.1021/acsomega.1c07307
ACS Omega 2022, 7, 15451−15458

Table 2. TE Properties of CaMgSi for Different Temperatures

T (K)	S (μV/K)	$\sigma \times 10^4$ (1/Ω m)	PF × 10−4 (W/m K^2)	$\tau \times 10^{-15}$ (s)	ke (W/m K)	kL (W/m K)	ZT_e	ZT
300	168.4766	1.8675	5.2647	15.172	0.1198	3.2906	1.3180	0.0477
400	199.1247	1.5012	5.9531	9.9693	0.1431	2.4931	1.6642	0.0905
500	210.0595	1.1999	5.2632	6.3841	0.1772	1.9933	1.4913	0.1215
600	200.9097	1.1294	4.5579	4.8591	0.2657	1.6606	1.0289	0.1418
700	171.3055	1.2573	3.6840	4.3655	0.4505	1.4232	0.5733	0.1382
800	120.8761	1.4836	2.1649	4.1702	0.7503	1.2452	0.2308	0.0855

calculated using the BoltzTraP code, which uses the approach called constant relaxation time approximation, which combines the electronic structure calculation and Boltzmann statistics. The obtained results were S, σ/τ, and k/τ, where the electrical and thermal conductivities are a function of the relaxation time τ.[26] A python script was developed to determine which simulated Seebeck values at fixed chemical potential best describe the experimental Seebeck (S_{Exp}) measurements using the least-squares method. The phonon band structure and phonon DOS were obtained using VASP and the density functional perturbation theory implemented in phonopy with a 2 × 3 × 2 supercell.[33,43] The phonon lifetime, Grüneisen parameters, and lattice thermal conductivity were obtained combining VASP and phono3py.[33,35] The VASP parameters are kinetic energy cutoff of 500 eV, a Monkhorst−Pack scheme in the Brillouin zone with 2 × 2 × 2 uniform k-point mesh, and the convergence energy threshold of 10^{-8} eV. The interatomic force constants in phono3py were determined using various positions of the atoms in a supercell made of 2 × 2 × 2 primitive cells.

AUTHOR INFORMATION

Corresponding Authors

Jesus L. A. Ponce-Ruiz − *Centro de investigación en Materiales Avanzados (CIMAV), Laboratorio Nacional de Nanotecnología, Chihuahua 31136, Mexico;* orcid.org/0000-0002-3123-1245; Email: jesus.ponce@cimav.edu.mx

J. M. Herrera-Ramirez − *Centro de investigación en Materiales Avanzados (CIMAV), Laboratorio Nacional de Nanotecnología, Chihuahua 31136, Mexico;* orcid.org/0000-0003-4321-6445; Email: martin.herrera@cimav.edu.mx

Authors

Seiya Ishizuka − *Toyohashi University of Technology, Department of Mechanical Engineering, Toyohashi, Aichi 441-8580, Japan*

Yoshikazu Todaka − *Toyohashi University of Technology, Department of Mechanical Engineering, Toyohashi, Aichi 441-8580, Japan*

Yuki Yamada − *Toyohashi University of Technology, Department of Mechanical Engineering, Toyohashi, Aichi 441-8580, Japan*

Armando Reyes Serrato − *Universidad Nacional Autónoma de México, Departamento modelación de nanomateriales, Centro de Nanociencias y Nanotecnología, Ensenada, Baja California 22860, Mexico*

Complete contact information is available at: https://pubs.acs.org/10.1021/acsomega.1c07307

Notes

The authors declare no competing financial interest.

ACKNOWLEDGMENTS

This work was partially supported by the project UNAM-PAPIIT-IG200320 and LANCAD-UNAM-DGTIC-084. The authors would like to thank Rodrigo Dominguez for the technical support of the computer cluster. Jesus L. A. Ponce Ruiz thanks CONACYT for the PhD scholarship (CVU-562553) and C. Koop-Santa for all the support. A.R.S. is grateful to Donostia International Physics Center (DIPC Donostia-San Sebastián, Spain) for their support during 2021 research stay.

REFERENCES

(1) Gorai, P.; Stevanović, V.; Toberer, E. S. Computationally Guided Discovery of Thermoelectric Materials. *Nat. Rev. Mater.* **2017**, *2*, 17053.

(2) Chen, Z.-G.; Han, G.; Yang, L.; Cheng, L.; Zou, J. Nanostructured Thermoelectric Materials: Current Research and Future Challenge. *Prog. Nat. Sci.: Mater. Int.* **2012**, *22*, 535−549.

(3) Yang, L.; Chen, Z. G.; Dargusch, M. S.; Zou, J. High Performance Thermoelectric Materials: Progress and Their Applications. *Adv. Energy Mater.* **2018**, *8*, 1701797.

(4) Kagdada, H. L.; Jha, P. K.; Śpiewak, P.; Kurzydłowski, K. J. Structural Stability, Dynamical Stability, Thermoelectric Properties, and Elastic Properties of GeTe at High Pressure. *Phys. Rev. B* **2018**, *97*, 134105.

(5) Reyes, A. M.; Ponce-Ruiz, J. L. A.; Hernández, E. S.; Serrato, A. R. Novel Thermoelectric Character of Rhenium Carbonitride, ReCN. *ACS Omega* **2021**, *6*, 18364−18369.

(6) Haque, E.; Rahaman, M. First-Principles Prediction of Structural Stability and Thermoelectric Properties of SrGaSnH. *RSC Adv.* **2021**, *11*, 3304−3314.

(7) Hong, M.; Lyv, W.; Li, M.; Xu, S.; Sun, Q.; Zou, J.; Chen, Z.-G. Rashba Effect Maximizes Thermoelectric Performance of GeTe Derivatives. *Joule* **2020**, *4*, 2030−2043.

(8) Hicks, L.D.; Dresselhaus, M. S. Thermoelectric figure of merit of a one-dimensional conductor. *Phys. Rev. B: Condens. Matter Mater.* **1993**, *47*, 16631.

(9) Minnich, A. J.; Dresselhaus, M. S.; Ren, Z. F.; Chen, G. Bulk Nanostructured Thermoelectric Materials: Current Research and Future Prospects. *Energy Environ. Sci.* **2009**, *2*, 466−479.

(10) Wang, X. W.; Lee, H.; Lan, Y. C.; Zhu, G. H.; Joshi, G.; Wang, D. Z.; Yang, J.; Muto, A. J.; Tang, M. Y.; Klatsky, J.; Song, S.; Dresselhaus, M. S.; Chen, G.; Ren, Z. F. Enhanced Thermoelectric Figure of Merit in Nanostructured n -Type Silicon Germanium Bulk Alloy. *Appl. Phys. Lett.* **2008**, *93*, 193121.

(11) Joshi, G.; Lee, H.; Lan, Y.; Wang, X.; Zhu, G.; Wang, D.; Gould, R. W.; Cuff, D. C.; Tang, M. Y.; Dresselhaus, M. S.; Chen, G.; Ren, Z. Enhanced Thermoelectric Figure-of-Merit in Nanostructured p-Type Silicon Germanium Bulk Alloys. *Nano Lett.* **2008**, *8*, 4670−4674.

(12) Hsu, K. F.; Loo, S.; Guo, F.; Chen, W.; Dyck, J. S.; Uher, C.; Hogan, T.; Polychroniadis, E. K.; Kanatzidis, M. G. Cubic AgPbmSbTe2+m: Bulk Thermoelectric Materials with High Figure of Merit. *Science* **2004**, *303*, 818−821.

(13) Poudel, B.; Hao, Q.; Ma, Y.; Lan, Y.; Minnich, A.; Yu, B.; Yan, X.; Wang, D.; Muto, A.; Vashaee, D.; Chen, X.; Liu, J.; Dresselhaus, M. S.; Chen, G.; Ren, Z. High-Thermoelectric Performance of

https://doi.org/10.1021/acsomega.1c07307
ACS Omega 2022, 7, 15451−15458

Nanostructured Bismuth Antimony Telluride Bulk Alloys. *Science* **2008**, *320*, 634−638.
(14) Yamanoglu, R.; Daoud, I.; Olevsky, E. A. Spark Plasma Sintering versus Hot Pressing−Densification, Bending Strength, Microstructure, and Tribological Properties of Ti5Al2.5Fe Alloys. *Powder Metall.* **2018**, *61*, 178−186.
(15) Gröbner, J.; Chumak, I.; Schmid-Fetzer, R. Experimental Study of Ternary Ca-Mg-Si Phase Equilibria and Thermodynamic Assessment of Ca-Si and Ca-Mg-Si Systems. *Intermetallics* **2003**, *11*, 1065−1074.
(16) Whalen, J. B.; Zaikina, J. V.; Achey, R.; Stillwell, R.; Zhou, H.; Wiebe, C. R.; Latturner, S. E. Metal to Semimetal Transition in CaMgSi Crystals Grown from Mg-Al Flux. *Chem. Mater.* **2010**, *22*, 1846−1853.
(17) Wu, H.; Zhou, W.; Udovic, T. J.; Rush, J. J. Structure and Hydrogenation Properties of the Ternary Alloys Ca2-XMgxSi ($0 \leq x \leq 1$). *J. Alloys Compd.* **2007**, *446*−*447*, 101−105.
(18) Hagihara, K.; Fujii, K.; Matsugaki, A.; Nakano, T. Possibility of Mg- and Ca-Based Intermetallic Compounds as New Biodegradable Implant Materials. *Mater. Sci. Eng., C* **2013**, *33*, 4101−4111.
(19) Niwa, Y.; Todaka, Y.; Masuda, T.; Kawai, T.; Umemoto, M. Thermoelectric Properties of Ca-Mg-Si Alloys. *Mater. Trans.* **2009**, *50*, 1725−1729.
(20) Miyazaki, N.; Adachi, N.; Todaka, Y.; Miyazaki, H.; Nishino, Y. Thermoelectric Property of Bulk CaMgSi Intermetallic Compound. *J. Alloys Compd.* **2017**, *691*, 914−918.
(21) Yang, J.; Fan, Q.; Ding, Y.; Cheng, X. Predicting Thermoelectric Performance of Eco-Friendly Intermetallic Compound p-Type CaMgSi from First-Principles Investigation. *J. Alloys Compd.* **2018**, *752*, 85−92.
(22) Miyazaki, H.; Inukai, M.; Soda, K.; Miyazaki, N.; Adachi, N.; Todaka, Y.; Nishino, Y. Electronic and Crystal Structures of Thermoelectric CaMgSi Intermetallic Compound. *J. Electron Spectrosc. Relat. Phenom.* **2016**, *206*, 18−23.
(23) Williamson, G. K.; Hall, W. H. X-Ray Broadening from Filed Aluminium and Tungsten. *Acta Metall.* **1953**, *1*, 22−31.
(24) Williamson, G. K.; Smallman, R. E. III Dislocation Densities in Some Annealed and Cold-Worked Metals from Measurements on the X-Ray Debye-Scherrer Spectrum. *Philos. Mag.* **1956**, *1*, 34−46.
(25) Tran, F.; Blaha, P. Accurate Band Gaps of Semiconductors and Insulators with a Semilocal Exchange-Correlation Potential. *Phys. Rev. Lett.* **2009**, *102*, 226401.
(26) Madsen, G. K. H.; Singh, D. J. A Code for Calculating Band-Structure Dependent Quantities. *Comput. Phys. Commun.* **2006**, *175*, 67−71.
(27) Zhu, X.-L.; Hou, C.-H.; Zhang, P.; Liu, P.-F.; Xie, G.; Wang, B.-T. High Thermoelectric Performance of New Two-Dimensional IV-VI Compounds: A First-Principles Study. *J. Phys. Chem. C* **2020**, *124*, 1812−1819.
(28) Joshi, T. K.; Shukla, A.; Sharma, G.; Verma, A. S. Computational Determination of Structural, Electronic, Optical, Thermoelectric and Thermodynamic Properties of Hybrid Perovskite CH3CH2NH3GeI3: An Emerging Material for Photovoltaic Cell. *Mater. Chem. Phys.* **2020**, *251*, 123103.
(29) Hayashi, D.; Nakai, Y.; Kyakuno, H.; Miyata, Y.; Yanagi, K.; Maniwa, Y. Temperature Dependence of the Seebeck Coefficient for Mixed Semiconducting and Metallic Single-Wall Carbon Nanotube Bundles. *Appl. Phys. Express* **2020**, *13*, 015001.
(30) Kumar Gudelli, V.; Kanchana, V.; Vaitheeswaran, G.; Svane, A.; Christensen, N. E. Thermoelectric Properties of Chalcopyrite Type CuGaTe2 and Chalcostibite CuSbS2. *J. Appl. Phys.* **2013**, *114*, 223707.
(31) McGaughey, A. J. H.; Jain, A.; Kim, H.-Y.; Fu, B. Phonon Properties and Thermal Conductivity from First Principles, Lattice Dynamics, and the Boltzmann Transport Equation. *J. Appl. Phys.* **2019**, *125*, 011101.
(32) Li, J.; Yang, J.; Shi, B.; Zhai, W.; Zhang, C.; Yan, Y.; Liu, P.-F. Ternary Multicomponent Ba/Mg/Si Compounds with Inherent Bonding Hierarchy and Rattling Ba Atoms toward Low Lattice Thermal Conductivity. *Phys. Chem. Chem. Phys.* **2020**, *22*, 18556−18561.
(33) Kresse, G.; Furthmüller, J. Efficiency of Ab-Initio Total Energy Calculations for Metals and Semiconductors Using a Plane-Wave Basis Set. *Comput. Mater. Sci.* **1996**, *6*, 15−50.
(34) Kresse, G.; Joubert, D. From Ultrasoft Pseudopotentials to the Projector Augmented-Wave Method. *Phys. Rev. B Condens. Matter* **1999**, *59*, 1758−1775.
(35) Togo, A.; Chaput, L.; Tanaka, I. Distributions of Phonon Lifetimes in Brillouin Zones. *Phys. Rev. B Condens. Matter* **2015**, *91*, 094306.
(36) Mion, C.; Muth, J. F.; Preble, E. A.; Hanser, D. Thermal Conductivity, Dislocation Density and GaN Device Design. *Superlattices Microstruct.* **2006**, *40*, 338−342.
(37) Chen, Z.; Jian, Z.; Li, W.; Chang, Y.; Ge, B.; Hanus, R.; Yang, J.; Chen, Y.; Huang, M.; Snyder, G. J.; Pei, Y. Lattice Dislocations Enhancing Thermoelectric PbTe in Addition to Band Convergence. *Adv. Mater.* **2017**, *29*, 1606768.
(38) Rietveld, H. M. A Profile Refinement Method for Nuclear and Magnetic Structures. *J. Appl. Crystallogr.* **1969**, *2*, 65−71.
(39) Roisnel, T.; Rodríquez-Carvajal, J.; WinPLOTR, J. A Windows Tool for Powder Diffraction Pattern Analysis. *Mater. Sci. Forum* **2001**, *378*−*381*, 118−123.
(40) Momma, K.; Izumi, F. VESTA 3 for Three-Dimensional Visualization of Crystal, Volumetric and Morphology Data. *J. Appl. Crystallogr.* **2011**, *44*, 1272−1276.
(41) Klinger, M.; Jäger, A. Crystallographic Tool Box (CrysTBox): Automated Tools for Transmission Electron Microscopists and Crystallographers. *J. Appl. Crystallogr.* **2015**, *48*, 2012−2018.
(42) Blaha, P.; Schwarz, K.; Tran, F.; Laskowski, R.; Madsen, G. K. H.; Marks, L. D. WIEN2k: An APW+lo Program for Calculating the Properties of Solids. *J. Chem. Phys.* **2020**, *152*, 074101.
(43) Togo, A.; Tanaka, I. First Principles Phonon Calculations in Materials Science. *Scr. Mater.* **2015**, *108*, 1−5.

https://doi.org/10.1021/acsomega.1c07307
ACS Omega 2022, 7, 15451−15458